New Generation Carboxyl Functionalized SiO$_2$ Nanocomposite Encapsulated with Nd^{3+}SIP Hydrogen Bonded Organic Framework (Ln^{3+}-HOF) Support for NIR-Luminescence

Mustafa Burak Coban[1] · **Elif Gungor**[1] · **Yasemin Acar**[1] · **Hulya Kara Subasat**[2]

Abstract

In this study, hydrothermally synthesized $\{[Nd(SIP)(H_2O)_4]\}_n$ (NdSIP) and carboxylate-modified SiO$_2$ spheres were used to obtain SiO$_2$@NdSIP nanocomposites. Different concentrations of NdSIP in the range of 5–15%wt. were used in the hydrothermal synthesis of SiO$_2$@NdSIP nanocomposites. NdSIP has been structurally characterized by single crystal X-ray diffraction technique. NdSIP and SiO$_2$@NdSIP nanocomposites were characterized using various techniques including field emission scanning electron microscopy (FESEM), thermogravimetric analysis (TGA), Hirshfeld surface analysis, Fourier transform infrared (FTIR), solid-state UV absorption and photoluminescence (PL) spectroscopy.

Keywords SiO$_2$ · Nd^{3+}-compounds · Crystal structure · Lanthanide hydrogen bonded-organic framework Ln-HOF · Hirschfeld surface analysis · Luminescence property

1 Introduction

In recent years studies on lanthanide-based hydrogen bonded-organic frameworks (Ln^{3+}-HOFs) as functional materials have great interest not only because of their interesting topologies but also because of their potential applications as multifunctional hybrids or nanocomposites in thermal stability and mechanical properties [1–7]. Unfortunately, although the chemistry of lanthanide compounds is attractive, their use in practical applications is still quite limited due to their mechanical and poor thermal properties. Therefore, lanthanide compounds attached to multiple organic or inorganic polymer structured hosts through physical doping or chemical bonding techniques are important processes to obtain lanthanide hybrids with superior properties [8]. Considering the versatile chemical modifications, lanthanide-based HOFs can be beneficially used to obtain

various nanocomposites or nanostructures [9]. The studies on lanthanide hybrid materials show that they have also a high potential for different applications such as optical waveguides, OLEDs, optical amplifiers, etc. [10]. Moreover, the placement of a lanthanide compound in a hybrid matrix also has a positive effect in terms of its thermal stability, luminescence output, superior mechanical properties and better processability [10–13]. Trivalent lanthanide ions (Ln^{3+}) have excellent photoactive properties, high luminescence quantum efficiencies and unique magnetic properties due to their 4f electrons. Nd^{3+} lanthanide ion is well known for its NIR luminescence and Nd^{3+} containing materials are the most popular luminescent materials for application in laser systems, organic liquid lasers, electroluminescent devices, NIR immunoassays and optical-fiber polymers [14].

The polymer nanocomposite materials are usually produced by techniques such as melt-mixing, in-situ polymerization, electrospinning, selective laser sintering and green chemistry that all aim to produce them with uniform dispersion and without aggregations [15]. In this study, among these techniques, the hydrothermal synthesis method, which is described as green chemistry, has been used to obtain both Nd^{3+}-HOF and SiO$_2$@NdSIP nanocomposites. Silica nanospheres are a suitable candidate for fluorescence sensors due to their highly sensitive stability and optical transparency [16, 17]. Additionally, replacing the interior of silica and

✉ Mustafa Burak Coban
  burakcoban@balikesir.edu.tr; khf.burak@gmail.com

[1] Faculty of Art and Sciences, Department of Physics, Balikesir University, TR-10145 Balikesir, Turkey

[2] Department of Energy, Molecular Nano-Materials Laboratory, Graduate School of Natural and Applied Sciences, Mugla Sitki Kocman University, Mugla, Turkey

solid sensor materials with –COOH groups in an uncomplicated procedure is extremely important for effective sensing processes [18]. Herein, the synthesis procedure, crystal structure, IR spectroscopy, thermogravimetric analysis (TGA), solid-state absorption, visible and NIR luminescence properties, Hirshfeld surface and morphologic properties of the compound were reported.

2 Experimental Studies

2.1 Materials and Physical Measurements

All chemicals and solvents used were of the highest purity and were used without further purification, as follows: Neodymium^{3+} nitrate hexahydrate (99.9%, Nd(NO$_3$)$_3$·6(H$_2$O)), 5-sulfoisophthalic acid monosodium salt (95%, NaH$_2$SIP), Tetraethoxysilane (≥99.0%, TEOS), 3-triethoxysilylpropylamine (95%, APTES), succinic anhydride, ammonia (p.a., 25 wt.-%), ethanol (HPLC grade), *N*,*N*-Dimethylformamide (anhydrous, 99.8%, DMF) were purchased from Sigma&Aldrich, and water was of Milli-Q grade (~18.3 mQ/cm). FT-IR spectra of the nanocomposites were performed on a PerkinElmer instrument in the range 600–4000 cm^{-1}. The PL spectra and the low-temperature spectra (LT) were measured using an ANDOR SR500i-BL luminescence spectrometer equipped with a triple grating and an intensified charge-coupled device (ICCD) camera as the visible range detector and InGaAs detector for NIR region. A frequency tripled Nd:YLFQ switched pulse laser at 349 nm was used as the excitation source. Thermo-gravimetry (TG) measurements were performed using Perkin Elmer STA 6000 thermal analyzer at a scan rate of 10 °C/min. The size and morphology of the nanocomposites were investigated with a Quanta 250 scanning electron microscope (SEM). A Philips PW-1710/00 device was employed to analyze the phase composition of the nanocomposite samples, using Cu Kα (λ=0.15406 nm) in the range 5°<2θ<50° in the θ–θ mode with a step of n s step (5 s<n<10 s) and a step width of 0.03°. A comparison between the experimental and calculated (from CIF's) PXRD patterns (see Fig. 4) was carried out with Mercury 3.9 [19].

2.2 Synthesis of [Nd(SIP)(H₂O)₄]ₙ (1)

The NdSIP compound was prepared by a similar method as reported in previous reports. A mixture of Nd(NO$_3$)$_3$·6(H$_2$O) (0.219 g, 0.5 mmol) and NaH$_2$SIP (0.134 g, 0.5 mmol) was placed in a Teflon-lined, 45 ml stainless steel autoclave containing 27 ml of distilled water. The autoclave was sealed,

heated for 72 h at 120 °C, and cooled to ambient temperature in open air. Light-purple prismatic crystals were obtained, washed thoroughly with deionized water and dried under ambient conditions.

2.3 Monodisperse SiO₂ Microspheres Fabrication

Monodisperse SiO$_2$ microspheres were synthesized by the modified Stöber process [20]. Silica particles were synthesized through the combination of 200 ml of ethanol, 16 ml of water, and 12 ml of ammonia. To the reaction beaker, 8 ml of TEOS was gradually added while the solution was stirred at ambient temperature. The beaker containing the reactants was left undisturbed on the stirrer for 24 h to allow the reaction to reach completion. Following this period, the products of hydrolysis and condensation reactions were observed to be relatively monodispersed silica particles. In order to remove any excess impurities, the resulting silica suspension was subjected to centrifugation and redispersion in ethanol three times, before being dried in an oven at a temperature of 80 °C for 24 h.

2.4 Surface Carboxyl-Modified SiO₂ Microspheres

The mixture of silane coupling agent APTES and succinic anhydride in stoichiometric ratios was evenly dispersed in DMF by stirring for 2 h at ambient conditions. Then, a suspension of silica in DMF with ultrasonic dispersion (20 mL), as well as deionized water (2 mL), was added to the above-mentioned solution, and the final mixture was allowed to stir overnight at ambient temperature. The final products were centrifuged and then washed with alcohol, which was repeated twice, drying in the oven. The resulting silica microspheres were functionalized with carboxylate.

2.5 Preparation of SiO₂@NdSIP (5–15%wt.) Compounds

In the synthesis, initially, NdSIP 0.03 g (for 5%wt.), 0.06 g (for 10%wt.) and 0.09 g (for 15%wt.) were dissolved in 12 mL DMF. A suspension containing carboxylate-functionalized silica microspheres (0.6 g) was dispersed in H$_2$O (2 mL) in a separate beaker and this suspension was added to the previous solution dropwise under stirring with the help of a micropipette. The mixture was sealed in a Teflon-lined stainless steel reactor and heated at 120 °C for 3 days. After the reaction, the system was slowly cooled down to room temperature. The solid products were collected via centrifugation. Finally, the products were washed several times with methanol and then air-dried overnight (see Scheme 1).
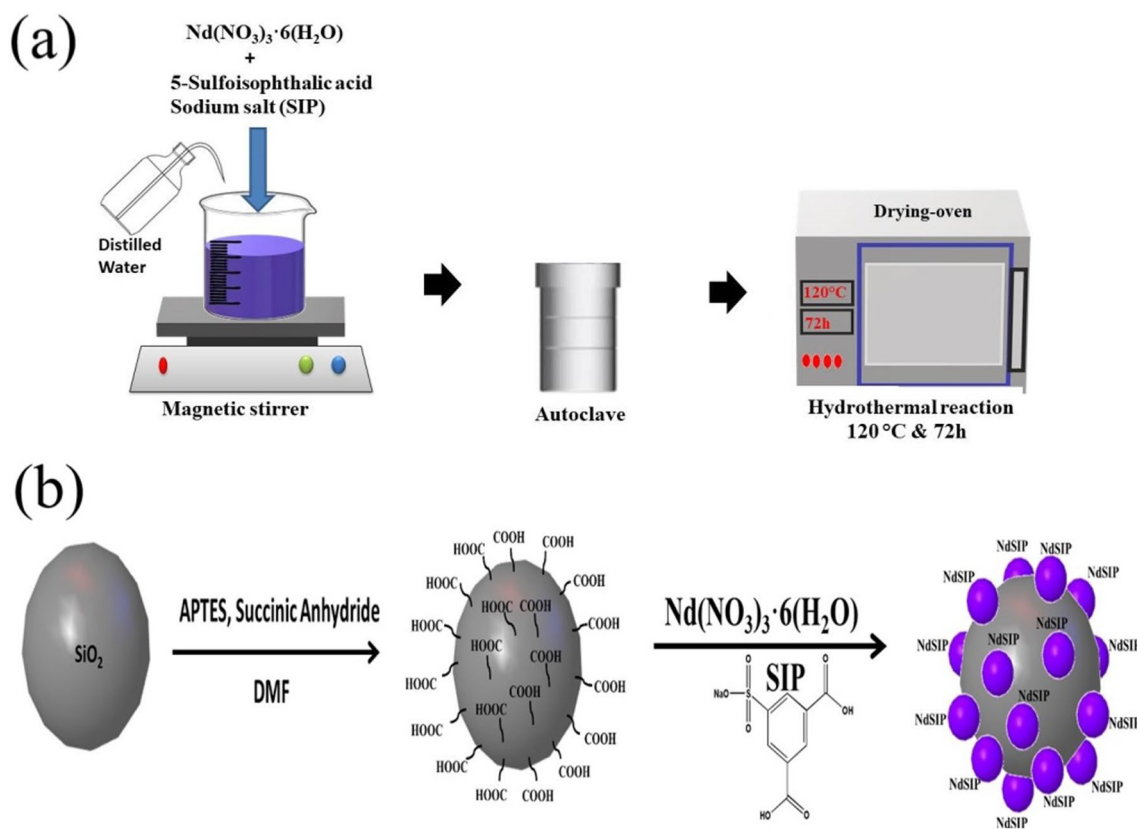
Scheme. 1. Outline of (**a**) NdSIP and (**b**) SiO$_2$@NdSIP nanocomposites generation process

2.6 X-Ray Structure Determination

A Single crystal of NdSIP with 0.32 mm×0.22 mm×0.13 mm was mounted on Rigaku-Oxford Xcalibur diffractometer with an Eos-CCD detector and its X-ray diffraction data has been collected using graphite monochromated Mo–Ka radiation ($\lambda = 0.71073$ Å). The dimensions of the crystal were determined during data collection using the CrysAlis^{Pro} software. The crystal image movie was recorded before starting data collection. Subsequently, the crystal center was appropriately defined in the face indexing section of the CrysAlis^{Pro} software. Consequently, the faces of the crystal were indexed using the methods available in the program (Point or Drag). The CrysAlis^{Pro} software [21] was used for data collection, cell refinement, data reduction, and analytical absorption corrections. The structure was solved using Direct Methods with the SHELXT [22] structure solution program and refined using Least Squares minimization with the SHELXL [23] refinement package in Olex2-1.5 [24]. The crystallographic and refinement data were shown in Table 1 while the selected bond lengths, bond angles and hydrogen bond geometry of the compound (**1**) were shown in Tables 2 and 3, respectively.

Table 1 The data collection and refinement parameters for NdSIP

CCDC	1886522
Formula sum	C$_8$H$_{11}$NdO$_{11}$S
Formula weight	459.47
Crystal system	Orthorhombic
Space group	$Pna2_1$
Unit cell dimensions	a = 7.3180 (4) Å
	b = 16.6509 (7) Å
	c = 10.4452 (5) Å
	$\alpha = \gamma = \beta = 90°$
Temperature (K)	296
Volume (Å^3)	1272.76
Z	4
ρ_{calc} (g/cm^3)	2.398
μ (mm^{-1})	4.30
Crystal size (mm)	0.32×0.22×0.13
Index ranges	− 8 ≤ h ≤ 8;
	− 19 ≤ k ≤ 18;
	− 12 ≤ l ≤ 11
Reflections collected	3809
Independent reflections	2104 [$R_{int} = 0.027$]
Parameters/restraints	153/1
S	1.09
Final R indexes [I > = 2σ (I)]	R$_1$ = 0.031; wR$_2$ = 0.071

Table 2 Some selected bond lengths [Å] and angles [°] for NdSIP

Bond lengths			
Nd1–O1	2.488 (7)	Nd1–O6	2.516 (7)
Nd1–O2	2.502 (10)	Nd1–O7	2.541 (12)
Nd1–O3	2.476 (8)	Nd1–O8	2.516 (12)
Nd1–O4	2.434 (11)	Nd1–O9	2.471 (8)
Nd1–O5	2.561 (8)		
Bond angles			
O1—Nd1—O2	140.9 (4)	O4–Nd1–O7	114.0 (3)
O1–Nd1–O5	75.9 (3)	O4–Nd1–O8	76.9 (3)
O1–Nd1–O6	71.7 (4)	O4–Nd1–O9	142.5 (4)
O1–Nd1–O7	72.2 (3)	O6–Nd1–O5	50.8 (3)
O1–Nd1–O8	80.0 (3)	O6–Nd1–O7	115.1 (3)
O2–Nd1–O5	138.9 (3)	O7–Nd1–O5	148.0 (3)
O2–Nd1–O6	139.5 (3)	O8–Nd1–O5	121.5 (3)
O2–Nd1–O7	72.0 (4)	O8–Nd1–O6	71.2 (3)
O2–Nd1–O8	89.2 (4)	O8–Nd1–O7	50.8 (3)
O3–Nd1–O1	131.9 (3)	O9–Nd1–O1	74.7 (3)
O3–Nd1–O2	69.5 (3)	O9–Nd1–O2	86.3 (3)
O3–Nd1–O5	70.5 (2)	O9–Nd1–O3	71.9 (3)
O3–Nd1–O6	109.0 (2)	O9–Nd1–O5	89.9 (3)
O3–Nd1–O7	135.1 (3)	O9–Nd1–O6	133.0 (3)
O3–Nd1–O8	147.4 (3)	O9–Nd1–O7	83.6 (3)
O4–Nd1–O1	141.0 (4)	O9–Nd1–O8	133.0 (3)
O4–Nd1–O2	69.9 (3)	O9–S1–O11	110.1 (5)
O4–Nd1–O3	72.7 (3)	O10–S1–O9	111.8 (5)
O4–Nd1–O5	89.9 (3)	O10–S1–O11	113.2 (5)
O4–Nd1–O6	71.3 (4)	S1–O9–Nd1	138.6 (5)

Table 3 Hydrogen bond geometry (Å, °) for NdSIP

D-H···A*	D-H	H···A	D···A	D-H···A
O1–H1A···S1	0.86	2.73	3.277 (12)	123
O1–H1A···O2^v	0.86	2.65	3.170 (15)	121
O1–H1A···O11	0.86	2.34	3.138 (13)	155
O2–H2A···O11^{vi}	0.86	2.17	2.927 (13)	146
O2–H2B···O1^{vi}	0.86	2.37	3.170 (15)	154
O3–H3A···O11^{vii}	0.91	2.20	2.813 (12)	124
O3–H3B···O5^{vii}	0.91	1.99	2.819 (11)	151
O4–H4A···O10^{viii}	0.93	2.37	3.035 (13)	129
O4–H4B···O1^{vi}	0.92	2.37	3.265 (15)	163
C6–H6···O4^{ix}	0.93	2.41	3.291 (15)	157

Symmetry codes: (v) $x-1$, y, z; (vi) $x+1$, y, z; (vii) $x+1/2$, $-y+1/2$, z; (viii) $-x+2$, $-y+1$, $z+1/2$; (ix) $x-1/2$, $-y+1/2$, $z-1$

3 Results

## 3.1 *Crystal Structure Description of $\{[Nd(SIP)(H_2O)_4]\}_n$ (1)*

NdSIP crystallizes in an orthorhombic crystal system with the $Pna2_1$ space group. The asymmetric unit of NdSIP consists of one SiO_2NdSIP molecule and four water molecules coordinated with the Nd^{3+} ion. As shown in Fig. 1, the Nd^{3+} center is nine-coordinated by four oxygen atoms from coordinated water molecules (O1, O2, O3, O4), four oxygen atoms from the carboxylate group of two different SIP ligands (O5, O6, O7, O8) and one oxygen atom from the sulfonate group of a third SIP ligand (O9). The coordination geometry of the NdO_9 core is shown in Fig. 1b. The $Nd-O_w$ bond length of the four oxygen atoms (O1, O2, O3, O4) from the coordinated water molecules are in the range 2.434 (11)- 2.502 (10) Å. The Nd-O bond length of the four oxygen atoms (O5, O6, O7, O8) of the carboxylate group of two different SIP ligands is in the range of 2.516 (7)- 2.561 (8) Å. The $Nd-OSO_3$ bond length of one oxygen atom (O9) of the sulfonate group of a third SIP ligand possessing a third SIP ligand is 2.471 (8) Å. Two of the three SIP ligands chelate to the Nd^{3+} ion via the carboxyl group, while the third ligand binds via an oxygen atom of the sulfonate group. All distances and angles are comparable to other nine-coordinate lanthanide-oxygen donor compounds reported previously [25, 26]. The bond lengths of S1-O9, S1-O10 and S1-O11 of **1** are 1.450(9) Å, 1.440(9) Å and 1.455(8) Å, respectively. These values are in the typical range of the S–O bond lengths in the sulphonate anion (1.40–1.49 Å) [25, 27]. The similarities of the three S–O bond lengths suggest that the strong conjugate at the sulphonate group dominates in the structure. The three SIP ligands are arranged around the central Nd^{3+} ion in a propeller-like manner.

Moreover, each SIP ligand is linked to three Nd^{3+} ions with two chelating carboxyl groups and one monodentate sulphonate group. Thus, it acts as a μ_3 bridging ligand connecting three metal atoms. As the structure proceeds in this way, an infinite 2D neutral Nd^{3+} organic framework with the formula $[Nd(SIP)(H_2O)_4]_n$ is formed. An extended view of this structure is shown in Fig. 2a. The extended structure is composed of $\{[Nd(H_2O)_4]_3(SIP)_3\}$ rings, which form a honeycomb appearance. These honeycomb-appearing rings are characterized by three interconnected nodes, alternating SIP ligands and Nd^{3+} coordination polyhedra.

**Fig. 1 a** The molecular structure of NdSIP. **b** View of the coordination geometry of the NdO$_9$ core of NdSIP

(a)

(b)
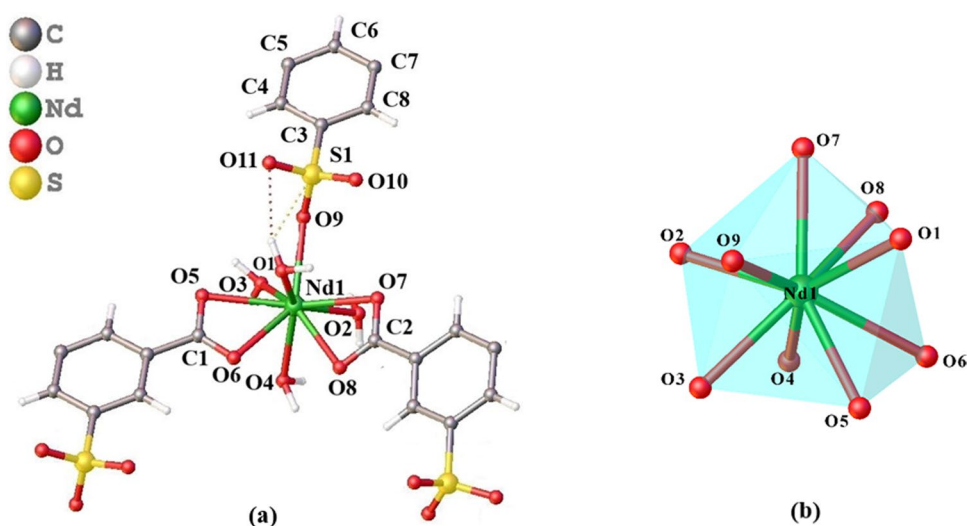
In the expanded structure, the layers in Fig. 1 are arranged from top to bottom and parallel to each other (Fig. 2b). The water molecules spread out like grass on both sides of the layers. The Nd^{3+} ions in one layer are located vertically above or below the center of the pseudo-hexagonal cavities of the other.

The crystal packing of NdSIP shows that the neighboring molecular are linked through intramolecular and intermolecular O – H···S, O – H···O and C – H···O hydrogen bonds (Table 3). These molecules are arranged in a 2D structure in the bc plane (Fig. 2). Additionally, 2D structures with hydrogen bond interactions are formed in 3D hydrogen-bonded organic frameworks in the *ab* plane and stacks along the *c*–axis (Fig. 3).

Meanwhile, the sample purity of SiO$_2$ and NdSIP doped SiO$_2$ composite samples were tested by XRD. The experimental PXRD patternof NdSIP are in good agreement with the simulated XRD model (CIF file obtained through crystal analysis), with slight shifts in the peak positions, which indicates the phase purity of compound. It indicates that the bulk NdSIP sample was isolated with high phase purity and the crystal structure was resolved correctly. Moreover, the structure of SiO$_2$ after coating with NdSIP, in comparison with the PXRD pattern obtained from pure NdSIP crystals, as evidence of the successful synthesis process. As we can see from Fig. 4, XRD peaks become more intense and narrow as the doping ratio increases.
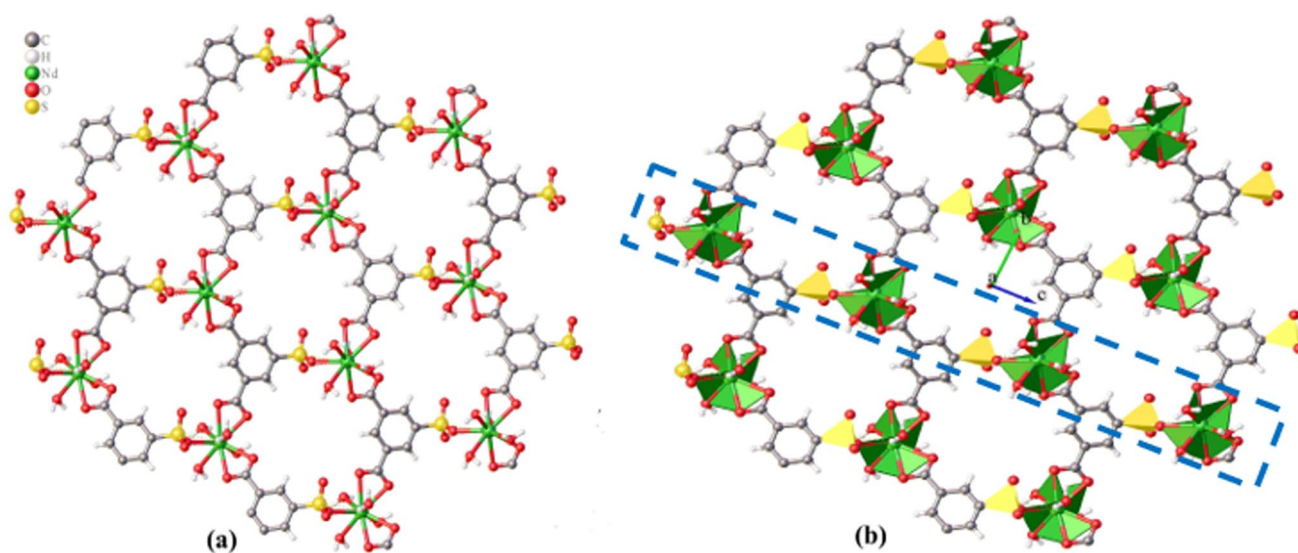
Fig. 2 (a) The infinite 2D neutral network which forms a honeycomb appearance in NdSIP and **(b)** Polyhedral representation in NdSIP
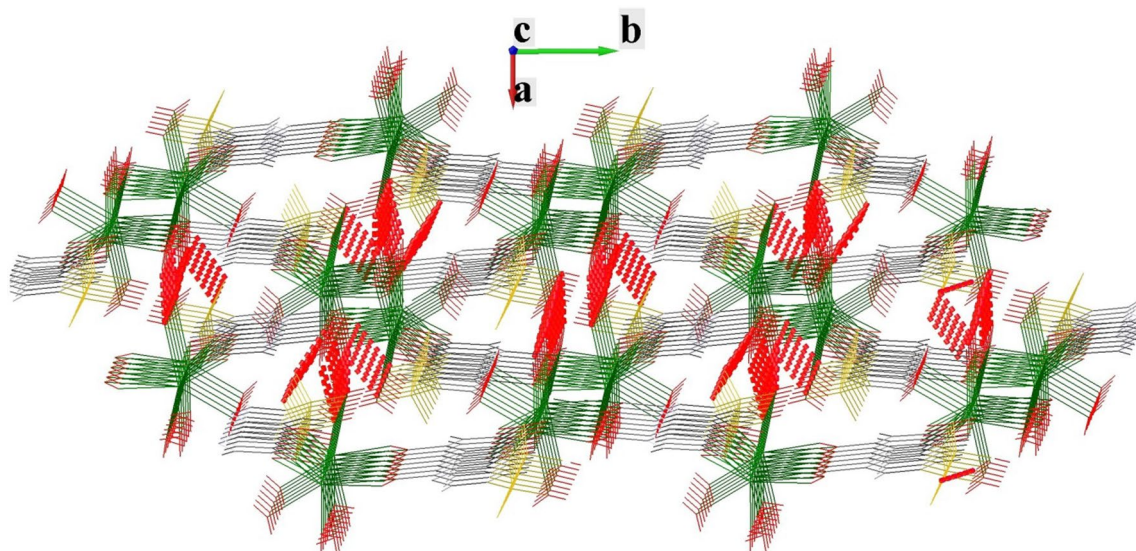
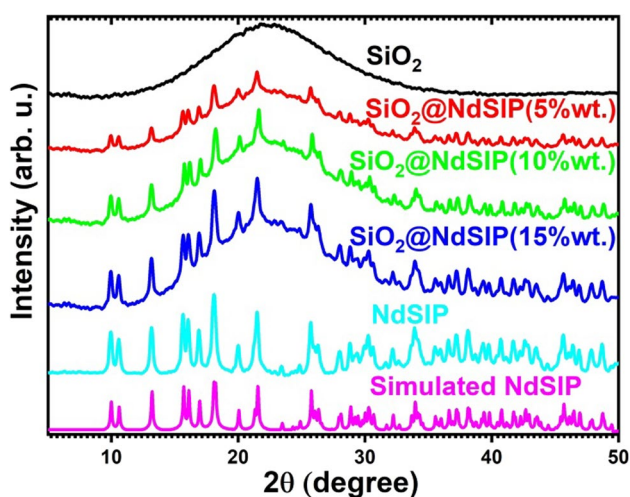**Fig. 3** 3D coordination network structure formed by hydrogen bonds of NdSIP

**Fig. 4** PXRD patterns of SiO$_2$, SiO$_2$@NdSIP (5, 10 and 15%wt.), NdSIP and simulated NdSIP

This indicates that the degree of crystallinity of the structure increases.

3.2 FTIR, SEM and TG Analysis

Figure 5 illustrates the infrared spectroscopy (FT-IR) results for the synthesized carboxyl-modified silica microspheres and SiO$_2$@NdSIP heterostructure microspheres. The increased intensity at 1045 cm^{-1}, attributed to the Si–O–Si (ν_{as}) peak, suggests the condensation of (3-aminopropyl) triethoxysilane (APTES) with Si–OH, and the presence of characteristic peaks at 2900–3500 cm^{-1} and 1649 cm^{-1} confirms the successful modification of the

SiO$_2$ surface with carboxyl groups [5, 8]. Additionally, the FT-IR spectrum of NdSIP exhibits a broad band centered at 3344 cm^{-1} and 1652 cm^{-1}, attributable to the presence of water molecules. The region 1100–1200 cm^{-1} displays strong characteristic absorptions for the sulfonate group of SIP^{3-} ligand, while the absence of O–H vibrations in the range of 1690–1730 cm^{-1} indicates that the carboxyl groups are completely protonated in NdSIP. The characteristic bands of carboxylate groups at 1530 cm^{-1} for asymmetric stretching vibration and at 1378 cm^{-1} in the usual region for symmetric stretching vibration indicate a bidentate bonding mode, which is consistent with the results of X-ray [25, 28, 29]. Furthermore, the bands at 784,724 and 620 cm^{-1} can be attributed to the C–H out-of-plane bending vibration of the phenyl group. When all the characteristic peaks in the FT-IR spectrum of SiO$_2$@ NdSIP are carefully evaluated, it is clear evidence of the successful preparation of SiO$_2$ doped nanocomposite structures [8, 30].

Scanning electron microscopy (SEM), an effective tool to observe the detailed morphology of all synthesized compounds has been extensively used. SEM micrographs of the coordination compound were carried out to understand their inner morphology, porosity and agglomerate situation. The morphology of the surface for the NdSIP compound clearly shows their crystalline nature exhibiting homogeneous rod-shaped crystals consisting of intercalated thin layers, as shown in Fig. 6a. Thus, the NdSIP compound exhibits good crystallinity character with rod-like structures with different thicknesses and lengths [31, 32]. Moreover, SEM images prove the formation of monodisperse and core–shell structures, as shown in Fig. 6b–c [5]. The particle size
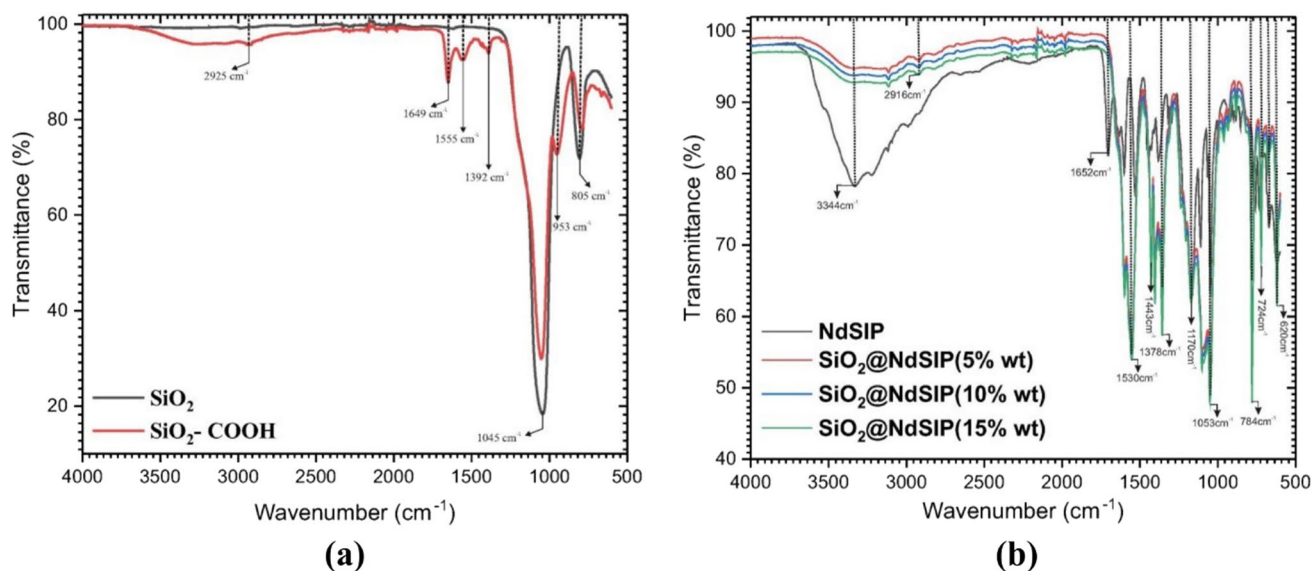
Fig. 5 FTIR Spectra of (**a**) SiO$_2$, SiO$_2$–COOH and (**b**) SiO$_2$@NdSIP(5–15%wt.), NdSIP nanocomposites
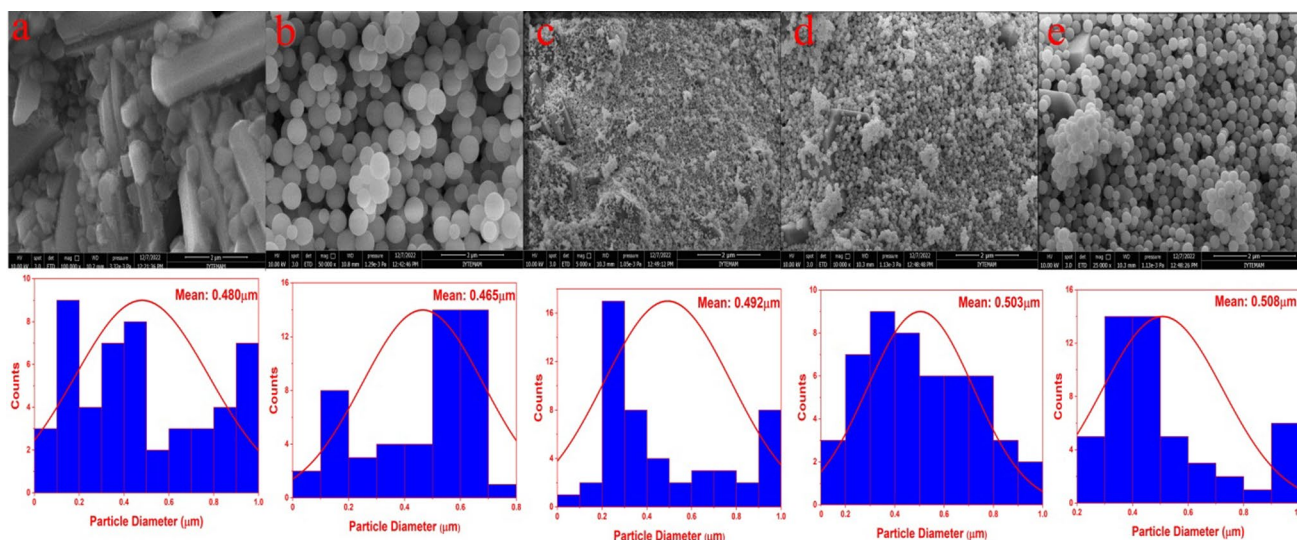
Fig. 6 SEM images of (**a**) NdSIP nanocomposite, (**b**) monodisperse SiO$_2$ and SiO$_2$@NdSIP (**c** 5%wt., **d** 10%wt. and **e** 15%wt.)

distribution histogram of NdSIP (Fig. 6a) and monodisperse microsphere (Fig. 6b) was constructed by analyzing approximately 100 particles with an average particle diameter of 480 and 465 nm, respectively. Moreover, the average particle size of SiO$_2$@NdSIP compound was observed in the range of 492–508 nm (5%wt. (Fig. 6c, 492 nm), 10%wt. (Fig. 6d, 503 nm) and 15%wt. (Fig. 6e, 508 nm)) [33]. Moreover, our observations show that NdSIP nanocomposite SiO$_2$ is encapsulated at different thicknesses on the monodisperse sphere surface. The average encapsulation thickness of monodisperse microspheres of NdSIP nanocomposites was determined in the range of 181–335 nm. As a result, increasing

doping concentration caused a significant thickness increase. As seen in XRD analyses, the increase in agglomeration levels, in SiO$_2$@NdSIP nanocomposites, confirms that they have a crystalline structure and that it is a successful doping process.

Thermogravimetric analysis (TGA) testing was performed on SiO$_2$ and NdSIP@SiO$_2$ nanocomposites to determine their stability. Thermogravimetric analysis of SiO$_2$, NdSIP and SiO$_2$@NdSIP (5, 10 and 15%wt.) were carried out at a heating rate of 10 °C min^{-1} under an N$_2$ atmosphere from 30 to 900 °C and TG curves are shown in Fig. 7. The thermal stability results of SiO$_2$ reveal that the compound's
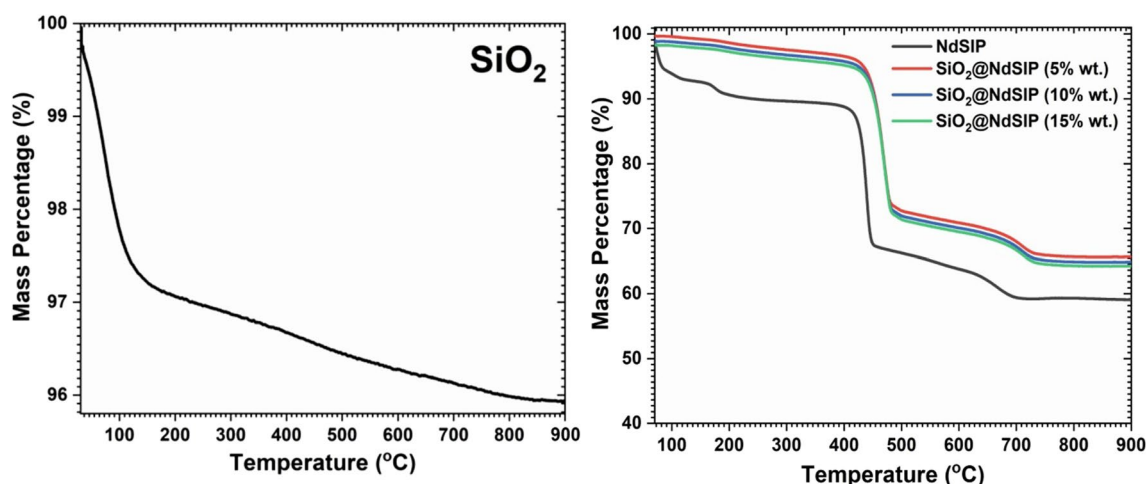
Fig. 7 TGA thermograms of SiO_2, NdSIP and SiO_2@NdSIP (5, 10 and 15%wt.)

slight weight loss between 50 and 160 °C is probably due to the physically combined humidity and/or water molecules adsorbed on the surface of nano-SiO_2. Another slight weight loss begins near 180 °C, continuing till 900 °C, which can be attributed to the silanol group dihydroxylation [34, 35].

As depicted in Fig. 7b, the thermogram of NdSIP reveals two stages of weight loss. The first stage of weight loss, from 30 to 150 °C, accounts for ~ 19–20% of the total weight loss, while the second stage, from 150 to 300 °C, accounts for approximately 2–5% of the weight loss. This suggests that the four coordinated water molecules of NdSIP are divided into two stages of weight loss. The TGA results indicate that the compounds are extremely stable and do not decompose until 400 °C. The anhydrous compounds remain stable up to ~ 400 °C, which can be attributed to the multidentate functionality of SIP and the rigidity of the extended polymeric structure. The weight loss temperature intervals for the undoped nanocomposites are calculated to be between 410 and 450 °C, which can be attributed to ligand decomposition and the coordination polymer framework beginning to collapse. Meanwhile, the NdSIP compound undergoes a slight weight loss above 700 °C, and the final residual weight is likely due to Nd^{3+} oxide [36–38]. Maximum thermal degradation temperatures were calculated according to TGA curves, which confirmed better thermal resistance. The parameter was reported as 430 and 410 °C for the NdSIP-modified SiO_2 and neat polymer, respectively. This trend can be attributed to the better compatibility of the components, resulting in improved thermal strength.

3.3 Hirshfeld Surface Analysis

The Hirshfeld surface analysis, a crucial technique for evaluating molecular arrangements and determining interactions within crystal structures, was conducted on the NdSIP compound using the CrystalExplorer 21.5 software [39]. The 3D Hirshfeld surfaces were mapped over dnorm, shape index, and curvedness, with the 2D fingerprint plots of the NdSIP compound, as shown in Fig. 8.

The dnorm parameter allows for the differentiation of regions participating in intermolecular interactions using color coding on the surface. In Hirshfeld surface maps, white, red, and blue colors have been utilized to represent shorter contacts, Van der Waals contacts, and longer contacts, respectively [40]. The red-colored region on the Hirshfeld surface is attributed to C–H⋯O type interactions, which are the most intense contacts near the surface, while the white-colored region is produced by intermediate atoms. The blue-colored region represents weaker contacts with longer distances [41].

The surface properties were assessed through shape index and curvedness mapping to determine the molecular arrangements in the crystal. The curvedness plots, as shown in Fig. 8c, contain valuable information about the π⋯π stacking of the molecule. The large green regions bordered by dark blue curves represent π⋯π stacking interactions of the molecules, while the flat areas of the surface indicate interactions between neighboring molecules. The C–H⋯π and O–H⋯π stacking information obtained from the shape index and curvedness plots is consistent with the crystal structure analyses.

The 2D fingerprint plots in Fig. 8d–i illustrate the intermolecular interactions in the NdSIP compound. The most significant interaction is O⋯H/H⋯O, contributing 44.2% to the NdSIP compound. O⋯H hydrogen bonding interactions play a major role in molecular packing. The other major contributions are H⋯H (21.2%), C⋯C (17.7%), O⋯O (9.6%), and C⋯H (5.8%) interactions. The blue-green regions on the fingerprint plots indicate the O–H⋯π and C–H⋯π interactions. Hirshfeld surface analysis showed the presence of
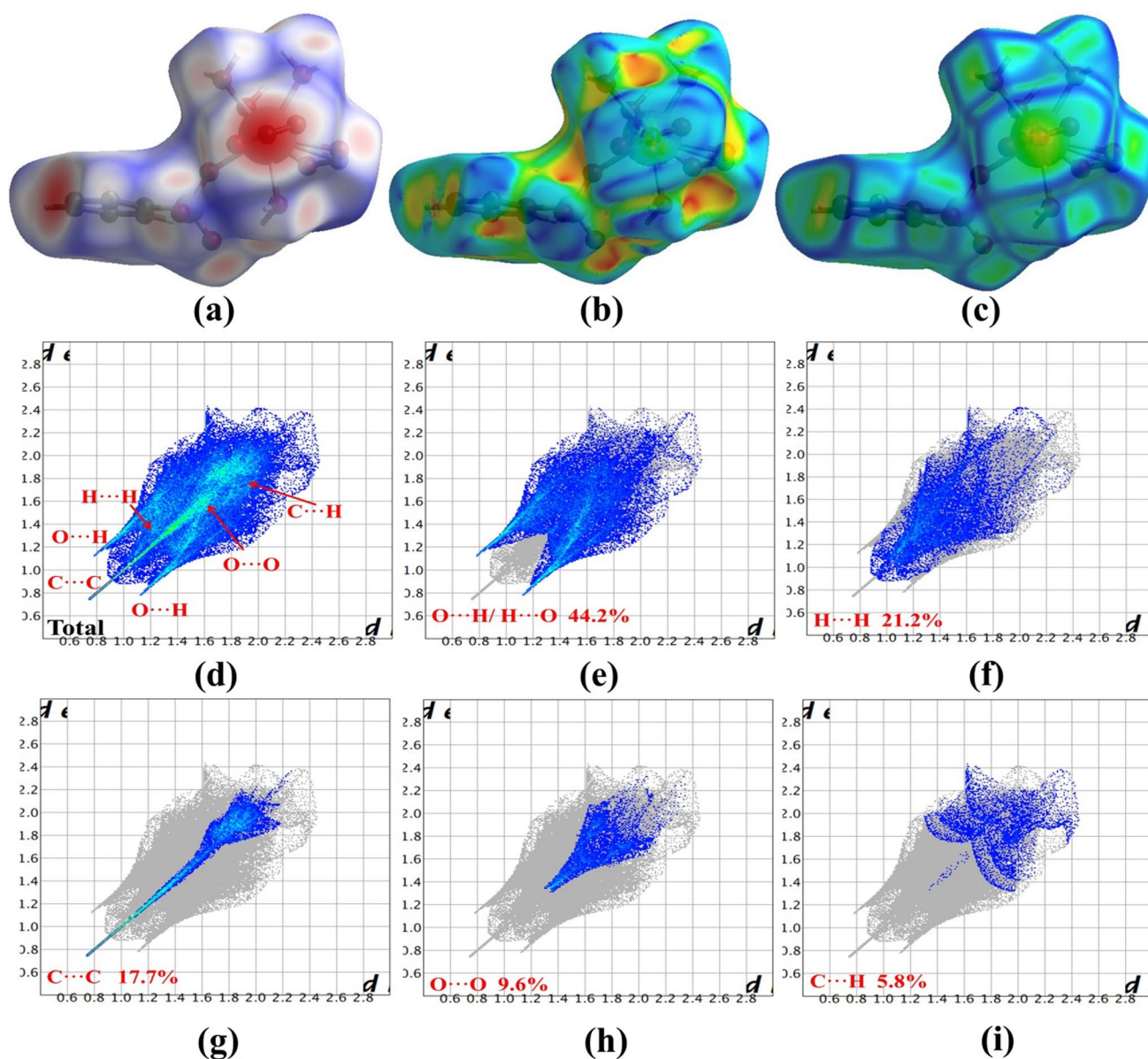
**Fig. 8** (**a**) Hirshfeld surface mapped with d_{norm} (**b**) shape index (**c**) curvedness and (**d–i**) 2D fingerprint plots of the compound **1**

O···H, H···H, C···C, O···O and C···H interactions, which is consistent with single crystal diffraction results.

3.4 Vis and NIR Luminescence Properties

According to Fig. 9, it can be seen that the SIP ligand and SiO_2 sample exhibit broadband emission in the case of photoluminescence. The solid-state emission spectra of the free NaH_2SIP ligands were recorded at room temperature, and it is noted that the free NaH_2SIP ligand emits blue light at 492 nm when excited by 349 nm, which is attributed to intraligand $n \rightarrow n^*$ or $\pi \rightarrow \pi^*$ transition [41–45]. In the case of SiO_2 luminescence spectrum, a weak and broad emission in the region of 400–700 nm is present, and a blue-light emission band at 497 nm is visible in the PL spectra. The blue light emission properties of SiO_2 have been studied in silicon nanocomposites produced in oxide matrices by several authors [46, 47]. Although the origin of the blue band is not entirely clear, it is generally believed to result from two oxygen atoms bonded to two-fold coordinated Si atoms. Tamura et al. have previously reported the presence of blue emission in porous silicon after oxidation [48]. The presence of luminescence centers in silica may be attributed to the interface of silicon ions and silica, or as isolated defects within the silica matrix. Our analysis of the luminescence observations,
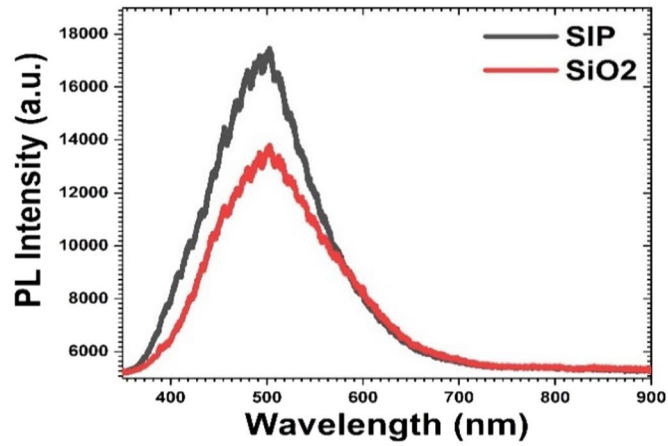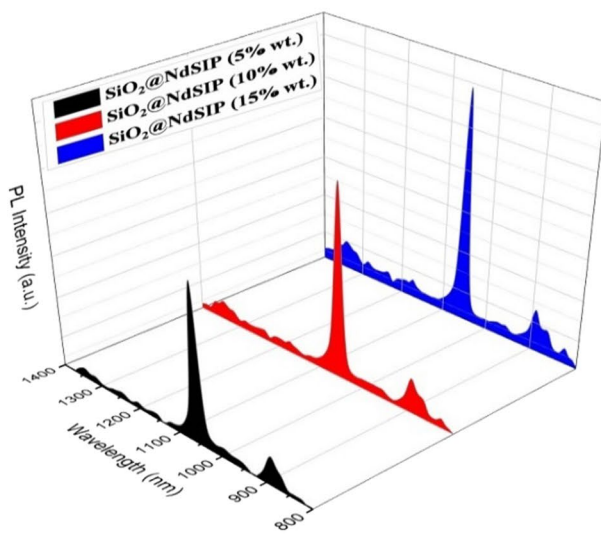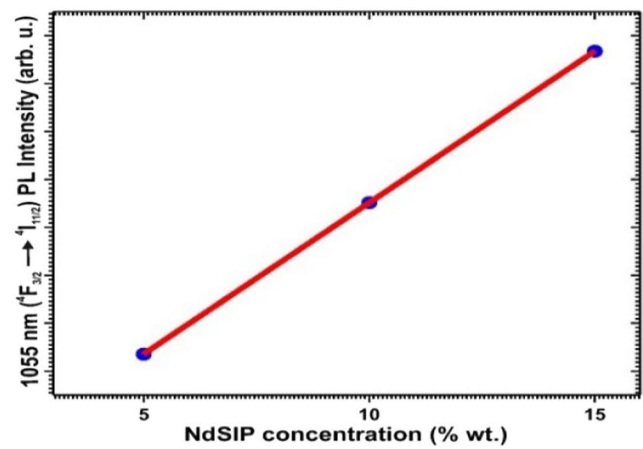
(a)
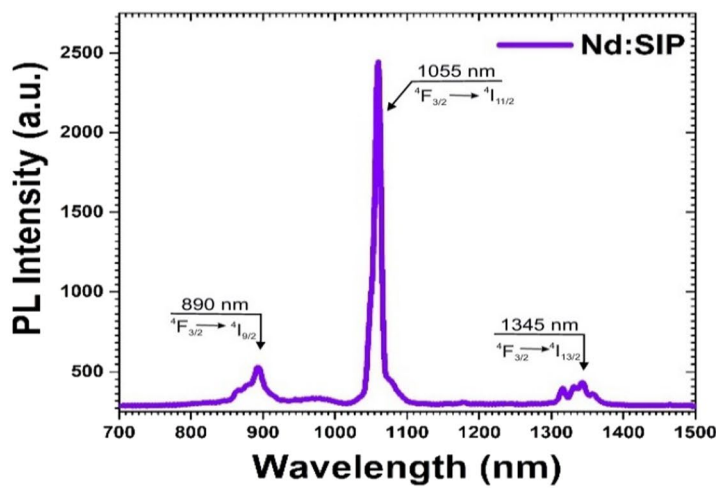
(b)
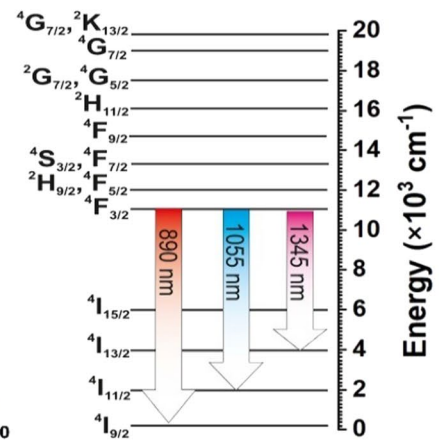
(c)

(d)

(e)

particularly the broad-band emission at room temperature, can be better explained by considering the blue-light emission band as resulting from quantum confined excitonic recombination in chains of silicon atoms or very small silicon nanocomposites. Further experimental analysis is necessary to gain a complete understanding of the origin of the blue-light emission band in the silica. The emission spectra of solid NdSIP and SiO$_2$@NdSIP (5–15%wt.) nanocomposites show strong emission bands in the range of 800–1400 nm at room temperature. The three intense peaks at 890, 1055, and 1345 nm correspond to the $^4F_{3/2} \rightarrow {}^4I_{9/2}$, $^4F_{3/2} \rightarrow {}^4I_{11/2}$, and $^4F_{3/2} \rightarrow {}^4I_{13/2}$ transitions of Nd^{3+} under 349 nm (Fig. 9c) [49–51]. The $^4F_{3/2} \rightarrow {}^4I_{11/2}$ (1055 nm) peak is the most intense and dominates the emission spectra of the compounds. The photoluminescence (PL) spectra of SiO$_2$@NdSIP nanocomposites were collected at different doping concentrations to observe the impact of doping on the PL spectrum, as shown in Fig. 9b. As evident in Fig. 9d, there is a simultaneous increase in the intensity of PL emission peaks with increasing doping concentration from 5% wt to 15% wt, indicating the influence of Nd^{3+} ions on enhancing the PL emission peak intensities.

The increase in photon-electron interactions within the material due to increased doping ions is attributed to the higher radiative recombination of excited carriers. This, in turn, leads to the excitation of more carriers, resulting in a higher intensity of PL peaks. In our comprehensive investigation of SiO$_2$@NdSIP, we used computational methodologies consistent with those reported in the literature. Our results, as depicted in Fig. 9d, e, reveal that the optimal doping concentration for Nd^{3+} ions in the SiO$_2$@NdSIP nanocomposite is precisely 15%wt. This concentration provides the right balance between the dopant concentration and material performance, making it the most conducive to enhancing PL properties. Furthermore, we examined the Nd^{3+} ion effect in SiO$_2$@NdSIP nanocomposites more effectively by evaluating the luminescence intensity as a function of temperature.

As demonstrated in Fig. 10, which depicts a typical collection of lines in the near-infrared region under laser excitation of 349 nm, the changes in photoluminescence with temperature can be easily observed through the three-dimensional (isometric) plots presented. Figure 9 allows for various viewing angles to be chosen, which can reveal key features that would otherwise be concealed.

Additionally, the process of monitoring the PL spectra and displaying the results as an intensity contour map as a function of temperature and emission wavelength provides valuable insights into understanding the PL processes from the NdSIP-doped SiO$_2$. Typically, Nd^{3+}-doped materials exhibit NIR emission. The room and low temperature (10 K) luminescence signals are displayed below for comparison, and it is evident that most of the emission at both temperatures falls within the 900–1350 range [52, 53]. Upon increasing the temperature, after an initial slow decline beginning around 100 K, the intensity of the Nd^{3+} $^4F_{3/2} \rightarrow {}^4I_{11/2}$ transitions decrease strongly over the 200–300 K range. This behavior can be attributed to the temperature-dependent phenomenon of thermal quenching.

3.5 Optical Evaluations

The optical absorbance and transmittance spectra for NdSIP and SiO$_2$@NdSIP (with 5%, 10%, and 15% weight concentration) nanocomposites are depicted in Fig. 11. The absorbance and transmittance spectral data in the wavelength range of 200–600 nm at ambient temperature have been collected to calculate a variety of optical parameters of these nanocomposites.

As seen in Fig. 11, the absorption spectra of all of the nanocomposites have sharp band at 212 nm and 284 nm and a shoulder band at 240 nm. The absorption in the 500–600 nm range is approximately stable for all of the nanocomposites. It shows that minimum absorbance is seen in 5% NdSIP doped SiO$_2$ nanocomposites and the maximum absorbance is seen in 15% NdSIP doped SiO$_2$ nanocomposites. When the absorbance graphs of the nanocomposites are compared with each other, it is seen that the absorbance values increase with increasing NdSIP concentration. Increasing the NdSIP concentration caused a slight blue shift in the absorption band. This can be attributed to the complexation between NdSIP and SiO$_2$ and the varying degree of crystallinity with increasing NdSIP concentration. Transmissions in the extended 200–600 nm spectral range are similar for all of the nanocomposites. But, there is a dramatic change from 250 to 350 nm in the ultraviolet for all of the nanocomposites. Additionally, transmittance (%) in the SiO$_2$@NdSIP nanocomposites decreases with increasing NdSIP concentration [54].

The absorption coefficient α (λ) is expressed by using the following equation [55]:

$$\alpha(\lambda) = 2.303x\frac{A}{d},$$

where A is the absorbance and d is the thickness of nanocomposites in this study.

Fig. 10 The isometric plot of temperature-dependent photoluminescence (PL) intensity as a function of wavelength and temperature, spanning the range from 10 to 300 K for SiO$_2$@NdSIP (15%wt.)
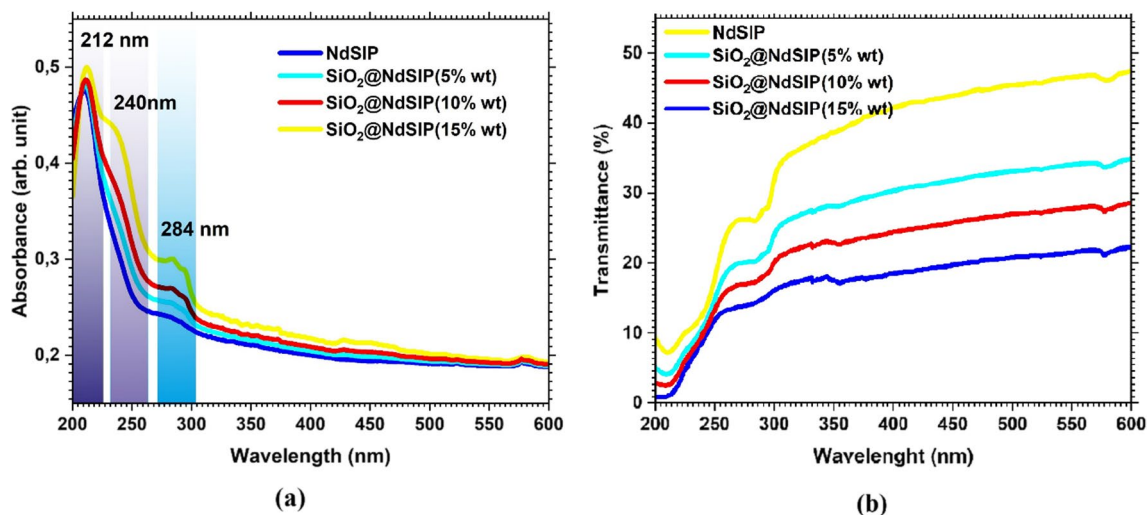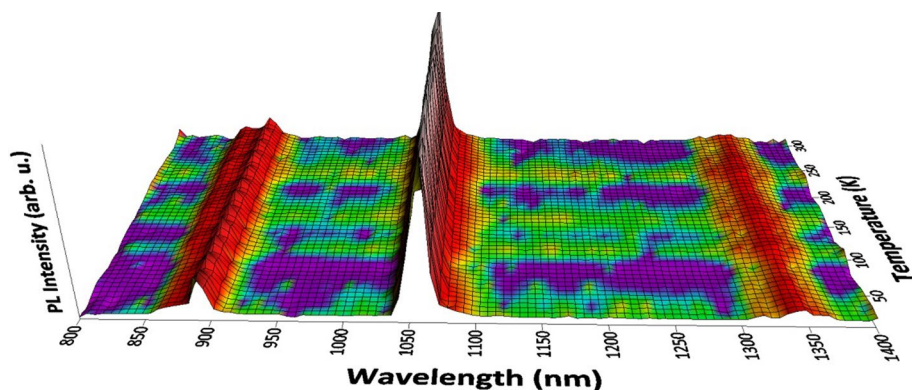
Fig. 11 (**a**) UV absorbance and (**b**) transmission spectra for NdSIP and SiO$_2$@NdSIP (5, 10 and 15% wt.) nanocomposites
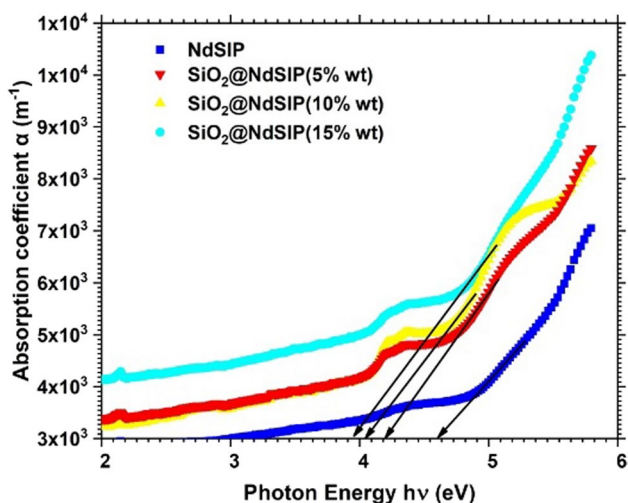
Fig. 12 Absorption coefficient (α) for NdSIP and SiO$_2$@NdSIP (5, 10 and 15% wt.) nanocomposites

Table 4 Optical energy gap of NdSIP and SiO$_2$@NdSIP (5, 10 and 15% wt.) nanocomposites

Nanocomposite	Absorption edge (eV)	E_{gi} (eV)	E_{gd} (eV)
NdSIP	4.61 eV	4.72	3.97
SiO$_2$@NdSIP (5%wt)	4.19	4.51	3.58
SiO$_2$@NdSIP (10%wt)	4.05	4.42	3.44
SiO$_2$@NdSIP (15%wt)	3.95	4.35	3.39

Figure 12 shows the variation of α as a function of the photon energy hν of the investigated nanocomposites. According to Fig. 12, the absorption coefficient of all nanocomposites shows almost a similar trend, and the absorbance coefficient of the nanocomposites increases as the photon energy (hν) increases. Here, it can be seen that the absorption coefficients for all nanocomposites are

distributed over all UV ranges. The investigation of the optical absorption edge is important because it provides valuable information about the band structure and optical band gap of the material. The study of the optical absorption edge is essential as it provides valuable information about the material's band structure and optical band gap [56–58]. The optical absorption edge values can be determined from the extrapolation of the linear section of the curves to zero absorption (Fig. 12; Table 4). As seen in Table 4, absorption edge energy values were found to be higher than 3 eV. These values are 4.61 eV for NIP, 4.19 eV for SiO_2@NdSIP (5%wt.), 4.05 eV for SiO_2@NdSIP (10%wt.) and 3.95 eV for SiO_2@NdSIP (15%wt.). The absorption coefficient of the nanocomposites increases with increasing NdSIP (5, 10 and 15% wt.) doping concentrations. The reason for the increase in the absorbance coefficient is probably an increase in the degree of structural disorder of the doped concentration [59, 60].

Optical absorption spectra of crystalline materials are used to determine the optical band gap energy. The direct and indirect optical band gaps of nanocomposite are calculated with the Tauc technique [61]. The optical band gap is found using the incident photon energy (hν) and the absorption coefficient (α) and can be expressed by the following equation [60, 61]:

$(h\nu - E_g)$.where h is Planck's constant, ν is the photon's frequency, α is the absorption coefficient, β is known as the disorder parameter which is energy independent and E_g is the optical band gap of investigated nanocomposites. The factor m depends on the electron transition and is equal to ½ for the direct transitions and 2 for the indirect transition band gaps. The $(\alpha h\nu)^2$ and $(\alpha h\nu)^{1/2}$ values have been plotted as a function of incident photon energy (hν) to determine the nature and width of the band gaps. The Fig. 13 shows

the dependence of $(\alpha h\nu)^2$ and $(\alpha h\nu)^{1/2}$ on photon energy hν for NdSIP compound and SiO_2@NdSIP (5, 10 and 15% wt.) nanocomposites. In Fig. 13, the linear segment of the relations is extrapolated to intersect the hν axis at the zero point to obtain the indirect band gap and direct band. The indirect and direct band gap values decrease with increasing NdSIP concentration as Table 4 and Fig. 13. The absorption coefficients of the investigated nanocomposites are around 10^1 cm^{-1}, and since the absorption coefficients are smaller than 10^4 cm^{-1}, the indirect transition is most likely [54, 60]. From Fig. 13, it can be seen that the indirect band gap E_g for the pure NdSIP blend is about 4.72 eV. The band gap of SiO_2@NdSIP (5, 10 and 15% wt.) nanocomposites with doped NdSIP have been determined as approximately 4.51 eV, 4.42 eV and 4.35 eV, respectively (Table 4). This decrease in the indirect optical band gap values is thought to be due to the formation of defects in the polymeric matrix and an increase in the degree of disorder in the nanocomposites with increasing NdSIP concentration [60]. The reduction of optical band gap is of great importance for polymeric materials. Because it is necessary for valuable applications and different potential optical device designs [60–64].

4 Conclusion

The production process of nanocomposites whose properties are examined in this study consists of three stages. The first is the synthesis of the Nd^{3+}-HOF by the hydrothermal method, the second is to obtain SiO_2 microspheres and modify them with carboxylate, and the third and final step is to obtain SiO_2@NdSIP nanocomposites by the hydrothermal method. X-ray structure analysis shows that the obtained
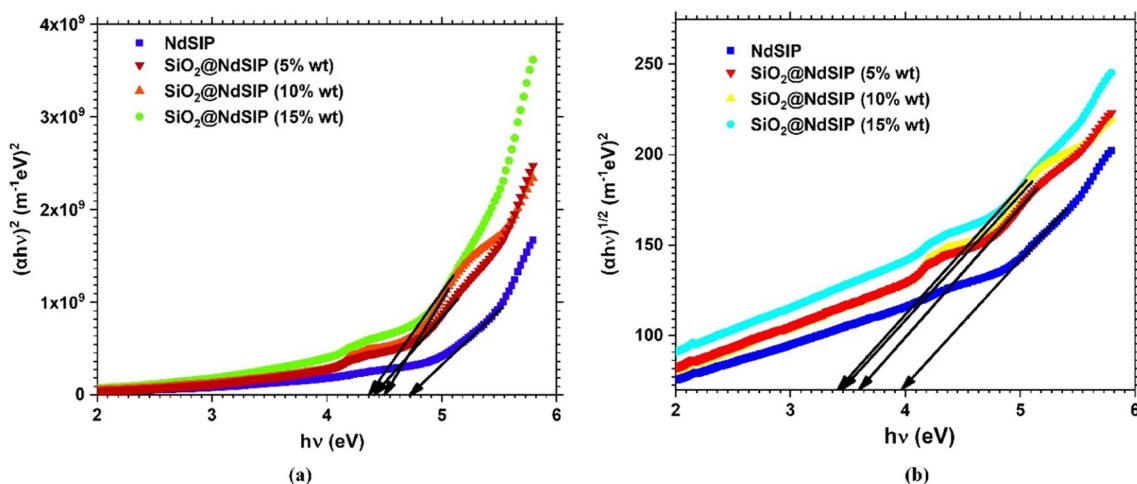
Fig. 13 (a) Plot of $(\alpha h\nu)^2$ vs. photon energy (hν) (indirect transition) and (b) Plot of $(\alpha h\nu)^{1/2}$ vs. photon energy (hν) (direct transition) for NdSIP and SiO_2@NdSIP(5, 10 and 15% wt.) nanocomposites

NdSIP compound formed a hydrogen-bonded-organic framework with a honeycomb appearance in two dimensions and also these 2D layers stacked in 3D via hydrogen bond interaction. The results of the Hirschfield analysis performed to determine the interactions and molecular arrangements in the crystal structure, consistent with single crystal x-ray, show $\pi \cdots \pi$ stacking of the molecules in the NdSIP compound and hydrogen bond interactions which play an important role in molecular packing. Different concentrations of NdSIP were added to observe their effects on the spectroscopic properties of SiO_2@NdSIP nanocomposites. When the FT-IR spectrum of SiO_2@NdSIP is examined, it is seen that the nanocomposites are doped with SiO_2 successfully. SEM images examined to understand the surface morphologies of the produced materials have revealed the rod-like crystalline nature of the NdSIP compound with different thicknesses and lengths and the formation of monodisperse SiO_2@NdSIP core–shell microspheres. In addition, with increasing doping concentration, the nanocrystalline nature of the synthesized nanocomposite was revealed and the agglomeration levels of spherical particles increased, as a result of which it was confirmed that they had a crystalline structure and the doping was successful. TGA curves examined for thermal stability show that SiO_2-doped nanocomposites have better thermal resistance than NdSIP compounds. This result also shows that the lanthanide compound in a hybrid matrix has a positive effect in increasing the thermal stability, as expected. The photoluminescence spectra of the free NaH_2SIP ligand and SiO_2 show blue light emission with the broadband at room temperature. To observe the doping effect, PL spectra of SiO_2@NdSIP nanocomposites were collected at different concentrations (range 5–15%wt.), and it was found that there was an increase in the intensity of PL emission peaks as the doping concentration increased by the effect of Nd^{3+} ions. This increase in PL intensity is because higher doped ions lead to more photon-electron interactions within the material, and therefore the higher doping rate causes more carriers to be excited. When the temperature-dependent photoluminescence (PL) intensity is examined, the decrease in the emission intensity of $Nd^{3+4}F_{3/2} \rightarrow {}^4I_{11/2}$ transitions with increasing temperature can be explained by the temperature dependence of thermal quenching.

The importance of this research lies in the necessity for further examination of NIR-luminescent materials and their properties across numerous fields, ranging from biological applications to information technology. A specific area of interest includes the study of lanthanide-doped luminescent materials, as the incorporation of a lanthanide compound in a matrix significantly enhances its thermal and (photo)chemical stability. The use of rare earth compounds doped SiO_2 is also beneficial due to their relatively low toxicity in biological media, excellent thermal, mechanical, and chemical

stability, and high optical performance. The increased stability of these compounds enables their use in NIR OLEDs, telecommunication applications, and luminescent probes.

Author contributions Mustafa Burak Coban: Project administration, Conceptualization, Methodology, Writing and original draft, Supervision, Software, Writing–original dra AQ ft, Writing—review and editing. Elif Gungor: Software, Visualization and Methodology. Yasemin Acar: Conceptualization, Visualization and Methodology. Hulya Kara Subasat: Software, Visualization and Methodology.

Data Availability Data will be made available on request.

Declarations

References

1. C. Molina, R.A.S. Ferreira, G. Poirier, L. Fu, S.J.L. Ribeiro, Y. Messsaddeq, L.D. Carlos, J. Phys. Chem. C **112**, 19346 (2008)
2. B. Yan, RSC Adv. **2**, 9304 (2012)
3. L. Guo, L. Fu, R.A.S. Ferreira, L.D. Carlos, Q. Li, B. Yan, J. Mater. Chem. **21**, 15600 (2011)
4. B.-H. Kwon, H.S. Jang, H.S. Yoo, S.W. Kim, D.S. Kang, S. Maeng, D.S. Jang, H. Kim, D.Y. Jeon, J. Mater. Chem. **21**, 12812 (2011)
5. X. Lian, B. Yan, Dalt. Trans. **45**, 2666 (2016)
6. J. Su, S. Yuan, Y.-X. Cheng, Z.-M. Yang, J.-L. Zuo, Chem. Sci. **12**, 14254 (2021)
7. H.-Y. Li, S.-Q. Zhang, M.-L. Chen, J.-H. Wang, Anal. Chem. **94**, 15448 (2022)
8. C. Liu, B. Yan, RSC Adv. **5**, 101982 (2015)

9. X.-T. Jiang, Q. Yin, B.-T. Liu, J.-Y. Chen, R. Wang, T.-F. Liu, Nanoscale Adv. **3**, 3441 (2021)
10. K. Binnemans, Chem. Rev. **109**, 4283 (2009)
11. L. Sun, L. Shi, Lanthanides: near-infrared materials, in Encycl. Inorg. Bioinorg. Chem. (John Wiley & Sons, 2012)
12. S. Comby, J.-C. G. Bünzli, Optical spectroscopy, in Handb. Phys. Chem. Rare Earths (North Holland, 2007), pp. 217–470
13. L.D. Carlos, R.A.S. Ferreira, V.Z. de Bermudez, S.J.L. Ribeiro, Adv. Mater. **21**, 509 (2009)
14. Y. Hasegawa, T. Ohkubo, K. Sogabe, Y. Kawamura, Y. Wada, N. Nakashima, S. Yanagida, Angew. Chemie Int. Ed. **39**, 357 (2000)
15. A. Kamal, M. Ashmawy, S. Shanmugan, A. Algazzar, A. Elsheikh, Proc. Inst. Mech. Eng. Part C J. Mech. Eng. Sci. **236**, 4843 (2022)
16. N. Dhiman, B.P. Singh, A.K. Gathania, Colloids Surfaces A Physicochem. Eng. Asp. **409**, 69 (2012)
17. I. Kumar, A. Kumar, S. Kumar, V. Sangwan, A.K. Gathania, IEEE Photonics J. **16**, 1 (2024)
18. N. Dhiman, A. Kumar, B.P. Singh, J. Nanophotonics **6**, 063511 (2012)
19. Mercury, version 3.9, Cambridge Crystallographic Data Centre, Cambridge, UK, 2016
20. A.K. Gathania, N. Dhiman, A. Sharma, B.P. Singh, Colloids Surfaces A Physicochem. Eng. Asp. **378**, 34 (2011)
21. CrysAlis[Pro], Rigaku Oxford Diffraction, Version 1.171.39.6a
22. G.M. Sheldrick, Acta Crystallogr. Sect. A Found. Adv. **71**, 3 (2015)
23. G.M. Sheldrick, Acta Crystallogr. Sect. C Struct. Chem. **71**, 3 (2015)
24. O.V. Dolomanov, L.J. Bourhis, R.J. Gildea, J.A.K. Howard, H. Puschmann, J. Appl. Crystallogr. **42**, 339 (2009)
25. Z. Wang, M. Ströbele, K.-L. Zhang, H.-J. Meyer, X.-Z. You, Z. Yu, Inorg. Chem. Commun. **5**, 230 (2002)
26. T. Qin, Z. Shi, W. Zhang, X. Dong, N. An, H. Sakiyama, M. Muddassir, D. Srivastava, A. Kumar, J. Mol. Struct. **1282**, 135220 (2023)
27. A. Onoda, Y. Yamada, M. Doi, T. Okamura, N. Ueyama, Inorg. Chem. **40**, 516 (2001)
28. T.K. Maiti, P. Dixit, J. Singh, N. Talapatra, M. Ray, S. Chattopadhyay, Int. J. Hydrogen Energy **48**, 1482 (2023)
29. X.-D. Zhu, K. Zhang, W.-X. Zhou, Q.-H. Li, Y.-Q. Fu, R.-M. Liu, G.-X. Qian, Inorg. Chem. Commun. **73**, 90 (2016)
30. M. Ferhi, S. Rahmani, A. Akrout, K. Horchani-Naifer, C. Charnay, J.O. Durand, M. Ferid, J. Alloys Compd. **764**, 794 (2018)
31. M.A. Kapadia, M.M. Patel, J.D. Joshi, Inorganica Chim. Acta **362**, 3292 (2009)
32. C. Cuerva, J. Tapiador, A.E. Sánchez-Peláez, M.C. Torralba, Á. Gutiérrez, Dye. Pigment. **181**, 108587 (2020)
33. L. Alcaraz, J. Isasi, Ceram. Int. **43**, 5311 (2017)
34. X. Gao, Y. Zhu, X. Zhao, Z. Wang, D. An, Y. Ma, S. Guan, Y. Du, B. Zhou, Appl. Surf. Sci. **257**, 4719 (2011)
35. X. Li, G. Wang, X. Li, Surf. Coatings Technol. **197**, 56 (2005)
36. M.B. Coban, E. Gungor, Y. Acar, F. Kuru Alpaslan, H. Kara Subasat, CrystEngComm **22**, 6116 (2020)
37. M.B. Coban, E. Gungor, Y. Acar, F.K. Alpaslan, H.K. Subasat, J. Mol. Struct. **1272**, 134117 (2023)
38. F. Kuru, M.B. Coban, U. Erkarslan, A. Donmez, G. Oylumluoglu, M. Aygun, H. Kara Subasat, Polyhedron **242**, 116492 (2023)
39. P.R. Spackman, M.J. Turner, J.J. McKinnon, S.K. Wolff, D.J. Grimwood, D. Jayatilaka, M.A. Spackman, J. Appl. Crystallogr. **54**, 1006 (2021)
40. O. Boukhemis, L. Bendjeddou, C. Platas-Iglesias, D. Esteban-Gómez, M. Carcelli, H. Merazig, Inorganica Chim. Acta **510**, 119740 (2020)
41. M.B. Coban, J. Solid State Chem. **317**, 123651 (2023)
42. H. Kara, G. Oylumluoglu, M.B. Coban, J. Clust. Sci. **31**, 701 (2020)
43. Y. Acar, M.B. Coban, E. Gungor, H. Kara, J. Clust. Sci. **31**, 117 (2020)
44. U. Erkarslan, A. Donmez, H. Kara, M. Aygun, M.B. Coban, J. Clust. Sci. **29**, 1177 (2018)
45. M.B. Coban, U. Erkarslan, G. Oylumluoglu, M. Aygun, H. Kara, Inorganica Chim. Acta **447**, 87 (2016)
46. H. Morisaki, H. Hashimoto, F.W. Ping, H. Nozawa, H. Ono, J. Appl. Phys. **74**, 2977 (1993)
47. S.H. Risbud, L.-C. Liu, J.F. Shackelford, Appl. Phys. Lett. **63**, 1648 (1993)
48. H. Tamura, M. Rückschloss, T. Wirschem, S. Veprek, Appl. Phys. Lett. **65**, 1537 (1994)
49. E. Cavalli, S. Ruggieri, S. Mizzoni, C. Nardon, M. Bettinelli, F. Piccinelli, Results Chem. **4**, 100388 (2022)
50. S.A. Bhat, K. Iftikhar, Opt. Mater. (Amst). **122**, 111660 (2021)
51. M. Iwamuro, Y. Wada, T. Kitamura, N. Nakashima, S. Yanagida, Phys. Chem. Chem. Phys. **2**, 2291 (2000)
52. V. Orsi Gordo, Y. Tuncer Arslanli, A. Canimoglu, M. Ayvacikli, Y. Galvão Gobato, M. Henini, N. Can, Appl. Radiat. Isot. **99**, 69 (2015)
53. T.H.Q. Vu, B. Bondzior, D. Stefańska, P.J. Dereń, J. Lumin. **257**, 119750 (2023)
54. F.M. Ali, R.M. Kershi, M.A. Sayed, Y.M. AbouDeif, Phys. B Condens. Matter **538**, 160 (2018)
55. A.Y. Yassin, A.-R. Mohamed, E.M. Abdelrazek, M.A. Morsi, A.M. Abdelghany, J. Mater. Res. Technol. **8**, 1111 (2019)
56. K. Kiran Kumar, M. Ravi, Y. Pavani, S. Bhavani, A.K. Sharma, V.V.R. Narasimha Rao, Phys. B Condens. Matter **406**, 1706 (2011)
57. B.M. Baraker, B. Lobo, J. Polym. Res. **24**, 84 (2017)
58. V. Raja, A. Sarma, V.V.R.N. Rao, Mater. Lett. **57**, 4678 (2003)
59. M.I. Abd-Elrahman, M.O. Ahmed, J.A. Abdel-Aleem, Mater. Sci. Semicond. Process. **16**, 1052 (2013)
60. M.B. Coban, M.E. Diken, S. Dogan, H. Kara Subasat, J. Inorg. Organomet. Polym. Mater. **33**, 2924 (2023)
61. S. Krishnaswamy, P. Panigrahi, S. Senthil Kumaar, G.S. Nagarajan, Nano-Struct. Nano-Obj. **22**, 100446 (2020)
62. K.S. Ojha, Optik (Stuttg). **127**, 2586 (2016)
63. R.P. Chahal, S. Mahendia, A.K. Tomar, S. Kumar, Appl. Surf. Sci. **343**, 160 (2015)
64. N.B. Rithin Kumar, V. Crasta, B.M. Praveen, Int. J. Struct. Integr. **6**, 338 (2015)